VIRTUAL AND PHYSICAL PROTOTYPING
2021, VOL. 16, NO. S1, S1–S18
https://doi.org/10.1080/17452759.2021.1922965

A numerical study on the packing quality of fibre/polymer composite powder for powder bed fusion additive manufacturing

Pengfei Tan[a], Fei Shen[b], Wei Shian Tey[a] and Kun Zhou [a]

[a]HP-NTU Digital Manufacturing Corporate Lab, School of Mechanical and Aerospace Engineering, Nanyang Technological University, Singapore; [b]Department of Mechanics, School of Mechanical Engineering, Tianjin University, Tianjin, People's Republic of China

ABSTRACT

A discrete element model has been developed to simulate the packing process of fibre/polymer composite powder for powder bed fusion additive manufacturing. The geometric shapes of polymer powder particles and fibres are represented by multi-sphere particles and individual cylinders with round ends, respectively. The numerical model can help to understand the flow dynamics of composite powder particles and the formation mechanisms of voids in powder packing processes. The numerical model has been utilised to analyse the effects of packing parameters on the packing quality of the powder bed. The simulation results suggest that the increase of the powder layer thickness is beneficial to the increase in the packing density and the decrease in the surface roughness of the powder bed. A high roller spreading velocity degrades the packing quality of the powder bed. Furthermore, a small number of fibres in the composite powder particles are in favour of the packing quality, but a further increase in the fibre number reduces it.

ARTICLE HISTORY
Received 19 January 2021
Accepted 24 April 2021

KEYWORDS
Additive manufacturing; Discrete element method; PA12; glass fibres; packing density; surface roughness

1. Introduction

Powder bed fusion (PBF) is one of the promising additive manufacturing techniques, where parts are built by fusing a powder bed via a layer-by-layer manner controlled by computer-aided design models. Because of its recent advances, PBF has been broadened into several branches such as selective laser melting, selective laser sintering, electron beam melting, and multi-jet fusion (Wu et al. 2017; Yuan, Chua, and Zhou 2019; Cai et al. 2021). PBF is suitable for producing a wide range of materials including metals, polymers, ceramics, and composites (Kuo et al. 2020; Nie et al. 2020; Yu, Sing, Chua, and Tian 2019). Additive manufacturing of fibre-reinforced polymer composites has gained great popularity because of its potential for improving and tailoring the mechanical properties of the printed parts. The main concerns in the manufacturing of high-quality composites are fibre orientation and void content in the composites (Parandoush and Lin 2017), which are strongly associated with the packing characteristics of powder beds such as packing density, surface roughness, and fibre homogeneity. Hence, there has been enormous attention paid to improving the packing quality of powder beds (Ziegelmeier et al. 2015; Parteli and Pöschel 2016; Haeri 2017; Gu, Xia, and Dai 2019).

Experimental studies have been conducted to investigate the powder flow dynamics and the packing characteristics of powder beds in additive manufacturing. Escano et al. (2018) applied in-situ X-ray imaging to capture the dynamic angle of repose (AOR) of a powder pile in a powder packing process, and suggested that the average particle size had major effects on the powder flow dynamics. Chen et al. (2019) measured the packing density and surface roughness of a powder bed, and experimental results were used to validate their numerical model. Owing to the difficulty in measuring the process variables such as particle velocity and contact force and exploring the underlying mechanisms in experiments, the discrete element method (DEM), proposed by Cundall and Strack (1979) for describing the motion behaviours and mechanical interactions of granular materials, has been employed to study the powder packing process in additive manufacturing (Steuben, Iliopoulos, and Michopoulos 2016; Xiang et al. 2016; Zohdi 2013). The DEM simulation gives insight into powder flow behaviours and helps to understand the interaction mechanisms of powder particles such as dragging (Haeri et al. 2017), jamming (Nan et al. 2018), segregation (Chen et al. 2019; Nan, Pasha, and Ghadiri 2020), and cohesion (Mier et al. 2019b) effects in the packing process.

CONTACT Kun Zhou kzhou@ntu.edu.sg HP-NTU Digital Manufacturing Corporate Lab, School of Mechanical and Aerospace Engineering, Nanyang Technological University, 50 Nanyang Avenue, Singapore 639798, Singapore

DEM simulations can provide guidance for improving the packing quality of powder beds, which is related to the packing parameters including the spreader type (Haeri et al. 2017), spreading velocity (Parteli and Pöschel 2016; Chen et al. 2020), powder layer thickness (Nan et al. 2018), powder size distribution (Parteli and Pöschel 2016; Chen et al. 2019; Meier et al. 2019b), and powder shape (Parteli and Pöschel 2016; Haeri et al. 2017; Schiochet Nasato and Pöschel 2020; Nan et al. 2018). Commercially available polymer powder usually has complex geometric shapes rather than a spherical one. The particle shape plays a vital role in the powder flow behaviours in the simulation of the packing process (Tian, Liu, and He 2020; Derksen 2020). To precisely represent the geometric shapes of powder particles, the multi-sphere method, in which particles of complex shapes are approximated by clumping several spheres, has been commonly applied (Parteli and Pöschel 2016; Haeri et al. 2017; Nan et al. 2018). In a reported DEM model (Haeri et al. 2017; Haeri 2017), the poly-ether ether ketone particles were approximated as roll-shape particles. Schiochet Nasato and Pöschel (2020) proposed a novel multi-sphere representation that retained the original template volume and flowability characteristics of arbitrarily shaped particles. They concluded that the particles with low aspect ratios could benefit the formation of compact powder beds at low recoating velocities, while spherical particles could perform better than elongated particles at high recoating velocities.

Fibre-reinforced polymer composites, the emerging materials for additive manufacturing, have found wide applications because of their superior features such as high strength to weight ratios, composition variability, and anisotropic mechanical properties (Yuan et al. 2019; Tan, Zhu, and Zhou 2020). The feasible PBF techniques that are commonly used for fabricating fibre-reinforced polymer composites include selective laser sintering and multi-jet fusion (Jansson and Pejryd 2016; Türk et al. 2017; Arai et al. 2018). The reinforced fibres of polymer composites exhibit the ability to improve their mechanical performance (Salazar et al. 2014; Parandoush and Lin 2017; Kathavate, Pawar, and Adkine 2019) and achieve anisotropic properties (Jansson and Pejryd 2016) in the printed parts. However, several challenges need to be addressed for PBF additive manufacturing of fibre-reinforced polymer composites, including pores, poor interlayer and fibre-polymer bonding, uncertain fibre orientation, and inhomogeneous fibre distribution (Parandoush and Lin 2017; Goh et al. 2019). These challenges are in high correlation with the packing characteristics of powder beds. The low packing density and large surface roughness of a powder bed may lead to the high porosity and delamination of the composite part. The orientation and distribution of fibres are predominantly determined in the packing process of the composite powder.

A high-quality powder bed is a prerequisite for obtaining satisfactory mechanical properties for the composite parts manufactured via PBF additive manufacturing. However, there is a lack of works on the packing process of composite powder. Herein, a DEM model is developed to simulate the packing process of fibre/polymer composite powder for PBF additive manufacturing. In this model, polymer powder particles and fibres are approximated by multi-sphere particles and individual cylinders with round ends, respectively. The particle contact is described by the viscoelastic Hertz-Mindlin theory, and the cohesive force due to the van der Waals force is also taken into account. The developed model is employed to investigate the effects of packing parameters, including the powder layer thickness, the roller spreading velocity, and the weight fraction of fibres, on the packing quality of the powder bed.

2. Discrete element model for fibre/polymer composite powder

The DEM model has been developed based on the open-source software YADE (Václav Šmilauer and Chareyre 2019). In the model, the contact interaction between particles is described by the Hertz-Mindlin theory that considers the damping force due to viscosity. The intermolecular cohesive force due to the van der Waals force is taken into account using the Derjaguin-Muller-Toporov (DMT) model. The polymer powder particles are approximated by multi-sphere particles based on the multi-sphere method, and the glass fibres are represented by cylinders with two round ends.

2.1. Discrete element model

In the DEM model, the translational and rotational motion of particles are derived using the Newton's second law (Cundall and Strack 1979):

$$\begin{cases} m\dfrac{\mathrm{d}\boldsymbol{v}}{\mathrm{d}t} = \boldsymbol{F} \\ I\dfrac{\mathrm{d}\boldsymbol{w}}{\mathrm{d}t} = \boldsymbol{M} \end{cases} \tag{1}$$

where m is the particle mass, $\boldsymbol{v}$ is the particle velocity, $\boldsymbol{F}$ is the total force acting on the particle, I is the moment of inertia, $\boldsymbol{w}$ is the angular velocity, and $\boldsymbol{M}$ is the total moment. The total force $\boldsymbol{F}$ is expressed as

$$\boldsymbol{F} = \boldsymbol{F}_{\mathrm{c}} + m\boldsymbol{g} + \boldsymbol{F}_{\mathrm{v}} \tag{2}$$

where $\boldsymbol{F}_c$ is the contact force, $\boldsymbol{g}$ is the gravitational acceleration, and $\boldsymbol{F}_v$ is the van der Waals force due to the intermolecular interaction.

A schematic of the contact interaction model is shown in Figure 1. The contact force can be decomposed into the normal component $\boldsymbol{F}_{cn}$ and the shear component $\boldsymbol{F}_{cs}$, which are expressed as (Tsuji, Tanaka, and Ishida 1992; Václav Šmilauer and Chareyre 2019)

$$\begin{cases} \boldsymbol{F}_{cn} = (k_n u_n + \eta_n v_{n,r})\boldsymbol{n}_n \\ \boldsymbol{F}_{cs} = \min\left(k_s u_s + \eta_s v_{s,r},\ \mu|\boldsymbol{F}_{cn}|\right)\boldsymbol{n}_s \end{cases} \tag{3}$$

where k_n is the normal stiffness of the material, u_n is the normal displacement, η_n is the normal damping coefficient, $v_{n,r}$ is the relative normal velocity, $\boldsymbol{n}_n$ is the unit vector in the normal direction, k_s is the shear stiffness, u_s is the shear displacement, η_s is the shear damping coefficient, $v_{s,r}$ is the relative shear velocity, μ is the coefficient of friction, and $\boldsymbol{n}_s$ is the unit vector in the shear direction. The normal stiffness k_n and shear stiffness k_s can be obtained by the following formulas (Thornton, Cummins, and Cleary 2013; Tsuji, Tanaka, and Ishida 1992):

$$\begin{cases} k_n = 2E^*\sqrt{R^* u_n} \\ k_s = 8G^*\sqrt{R^* u_n} \\ E^* = \left(\dfrac{1-\upsilon_1^2}{E_1} + \dfrac{1-\upsilon_2^2}{E_2}\right)^{-1} \\ R^* = \left(\dfrac{1}{R_1} + \dfrac{1}{R_2}\right)^{-1} \\ G^* = \left(\dfrac{2-\upsilon_1}{G_1} + \dfrac{2-\upsilon_2}{G_2}\right)^{-1} \end{cases} \tag{4}$$

where the superscript * denotes the effective material properties of two interacting particles, the subscripts 1 and 2 indicate the two interacting particles, E is the Young's modulus of the material, R is the radius of the particle, υ denotes the Poisson's ratio, and the shear modulus $G = \mathrm{E}/(2(1+\upsilon))$. The damping coefficients η_n and η_s are expressed as

$$\begin{cases} \eta_n = 2\sqrt{\dfrac{5}{6}}\beta\sqrt{m^* k_n} \\ \eta_s = \eta_n \\ \beta = \dfrac{|\ln\lambda|}{\sqrt{\ln^2\lambda + \pi^2}} \end{cases} \tag{5}$$

where $m^* = m_1 m_2/(m_1+m_2)$ is the effective mass with m_1 and m_2 being the mass of two interacting particles, respectively, and λ is the coefficient of restitution.

The DMT model is employed to calculate the van der Waals force of the polymer particles (Derjaguin, Muller, and Toporov 1975):

$$\boldsymbol{F}_v = -4\pi R^* \gamma \boldsymbol{n}_n \tag{6}$$

where γ is the surface energy density of the material.

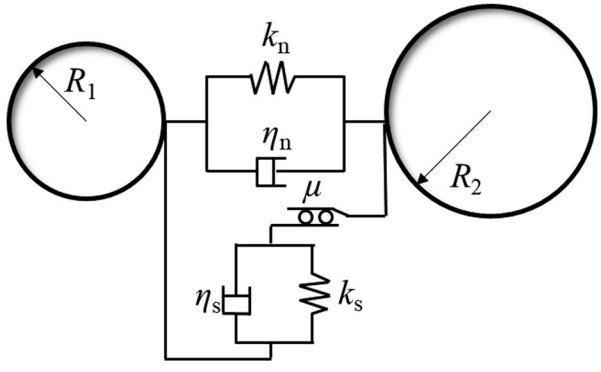

Figure 1. Schematic of the contact model (Modenese 2013; Tsuji, Tanaka, and Ishida 1992).

2.2. Polymer powder

Commercially available polyamide 12 (PA12) powder particles demonstrate complex non-spherical shapes, as shown in Figure 2(a). The particle size distribution of PA12 powder is given in Figure 2(b). A multi-sphere method, by which multiple spheres with the same or different sizes are clumped to approximate the irregularly shaped particle, is employed to create the non-spherical particles in the model. Several representative particle models are illustrated in Figure 2(c). Herein, the particle size refers to the minimum diameter of the sphere that can enclose the non-spherical particle. To exclude the spherical members with too small diameters in the multi-sphere particles and thus increase the computational time step, only the first five shapes in Figure 2 (c) are selected and equally allocated to model the particles with sizes smaller than 35 μm. When the particle size is larger than 35 μm, all the nine representative particle shapes are equally used.

To correctly describe the motion of the non-spherical particles, the mass m_c and the moment of inertia I_c need to be properly calculated by considering the overlap volume between the members of the clump. The particle is assumed to be confined inside an axis-aligned bounding box that is discretized by uniform grids. The parameters m_c and I_c are then calculated by summing over the cells of the discretized bounding box (Václav Šmilauer and Chareyre 2019):

$$\begin{cases} m_c = \sum_i m_i \\ I_c = \sum_i (m_i d_i^2 + I_i) \end{cases} \tag{7}$$

where m_i is the mass of cell i, d_i is the distance between the centre of the cell and the mass centre of the particle,

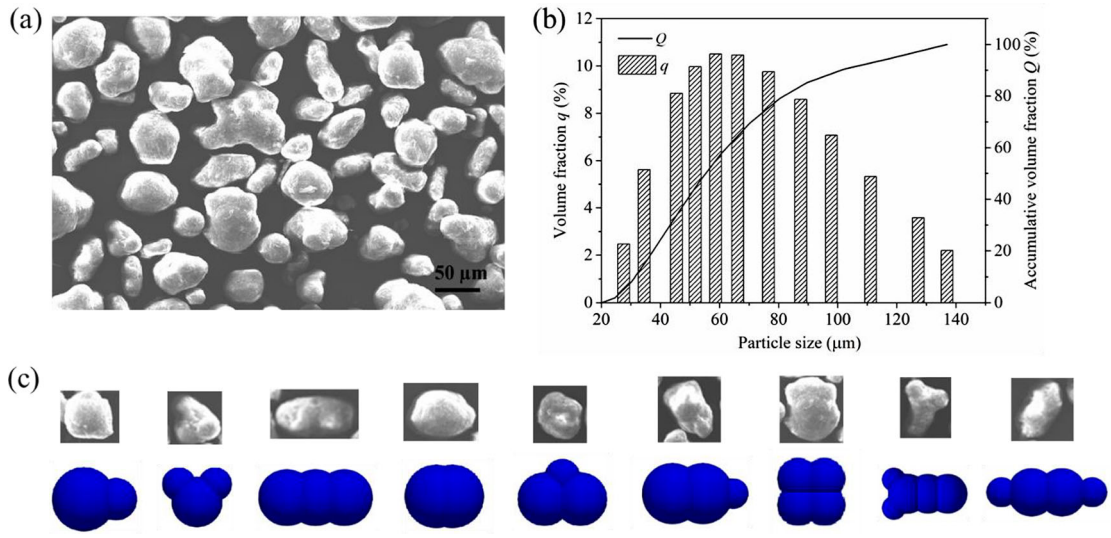

Figure 2. (a) Microscopic image of PA12 powder, (b) particle size distribution of PA12 powder, and (c) multi-sphere particles.

and I_i is the inertia of the cell. The force $\boldsymbol{F}_c$ and torque $\boldsymbol{T}_c$ of the particle are also obtained from the members of the clump (Václav Šmilauer and Chareyre 2019):

$$\begin{cases} \boldsymbol{F}_c = \sum_j \boldsymbol{F}_j \\ \boldsymbol{T}_c = \sum_j (\boldsymbol{r}_j \times \boldsymbol{F}_j + \boldsymbol{T}_j) \end{cases} \tag{8}$$

where $\boldsymbol{F}_j$ is the force applied to member j, $\boldsymbol{r}_j$ is the position vector of the member, and $\boldsymbol{T}_j$ is the torque on the member.

2.3. Glass fibres

The microscopic image of glass fibres is shown in Figure 3(a). In the DEM model, the geometric shape of glass fibres is approximated by a spherocylinder that is the combination of a sphere and a cylinder, as shown in Figure 3(b). The two ends of the cylinder are assumed to be two interaction nodes. The bond forces and moments due to the interaction of the two end nodes of the fibre are expressed as (Kunhappan et al. 2017; Bourrier et al. 2013; Effeindzourou et al. 2016)

$$\begin{cases} \boldsymbol{F}_n^b = k_n^b(l - l_0)\boldsymbol{n}_c, & \mathrm{d}\boldsymbol{F}_s^b = k_s^b \boldsymbol{v}_s^b \mathrm{d}t \\ \mathrm{d}\boldsymbol{M}_t^b = k_t^b \boldsymbol{\omega}_t \mathrm{d}t, & \mathrm{d}\boldsymbol{M}_b^b = k_b^b \boldsymbol{\omega}_b \mathrm{d}t \\ k_n^b = \dfrac{E_c \pi r_c^2}{l}, & k_s^b = \dfrac{3E_c \pi r_c^4}{l^3} \\ k_t^b = \dfrac{G_c \pi r_c^4}{2l}, & k_b^b = \dfrac{E_c \pi r_c^4}{4l} \end{cases} \tag{9}$$

where $\boldsymbol{F}_n^b$ and $\boldsymbol{F}_s^b$ are the bond forces in the normal and shear direction, respectively; l is the length of the fibre;

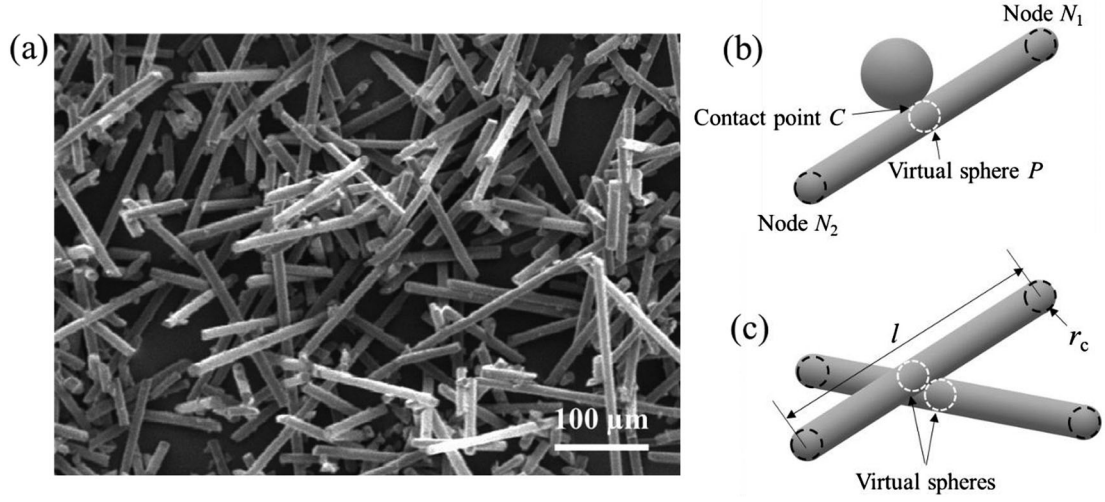

Figure 3. (a) Microscopic image of glass fibres and illustrations of the (b) polymer particle–fibre interaction and (c) fibre–fibre interaction.

l_0 is the length of the fibre at free conditions; $\boldsymbol{n}_c$ is the normal unit vector; $\boldsymbol{v}_s^b$ is the relative tangential velocity; $\boldsymbol{M}_t^b$ and $\boldsymbol{M}_b^b$ are the moments due to twisting and bending, respectively; $\boldsymbol{\omega}_t$ and $\boldsymbol{\omega}_b$ are the components of the relative angular velocity due to twisting and bending, respectively; E_c is the elastic modulus of the fibre; r_c is the radius of the fibre; G_c is the shear modulus of the fibre.

The schematics of the polymer particle – fibre and fibre – fibre interactions are illustrated in Figure 3(b) and (c), respectively. In Figure 3(b), a virtual sphere P is introduced in the cylinder for considering the contact with the polymer particle. The centre of the virtual sphere with the same radius as the cylinder is located at the projection of the contact point C on the axis of the cylinder. The polymer – fibre contact and fibre – fibre contact are transformed into virtual sphere – spherical polymer particle interaction and virtual sphere – virtual sphere interaction, respectively. The translational velocity $\boldsymbol{v}$ and angular velocity $\boldsymbol{\omega}$ of the virtual sphere are assumed to linearly vary between the two end nodes N_1 and N_2 of the cylinder (Bourrier et al. 2013; Effeindzourou et al. 2016):

$$\begin{cases} \boldsymbol{v} = (1-\xi)\boldsymbol{v}_1 + \xi\boldsymbol{v}_2 \\ \boldsymbol{\omega} = (1-\xi)\boldsymbol{\omega}_1 + \xi\boldsymbol{\omega}_2 \\ \xi = \dfrac{|\boldsymbol{N}_1 - \boldsymbol{P}|}{|\boldsymbol{N}_1 - \boldsymbol{N}_2|} \end{cases} \tag{10}$$

where the subscripts 1 and 2 indicate the two end nodes; $\boldsymbol{N}_1$ and $\boldsymbol{N}_2$ are the position vectors at nodes N_1 and N_2, respectively; $\boldsymbol{P}$ is the centre position vector of the virtual sphere. The contact force $\boldsymbol{F}_P$ and torque $\boldsymbol{T}_P$ that are applied to the virtual sphere are distributed on the two end nodes of the cylinder by using the following transformation:

$$\begin{cases} \boldsymbol{F}_1 = \boldsymbol{F}_P(1-\xi), & \boldsymbol{F}_2 = \boldsymbol{F}_P\xi \\ \boldsymbol{T}_1 = \boldsymbol{T}_P(1-\xi), & \boldsymbol{T}_2 = \boldsymbol{T}_P\xi \end{cases} \tag{11}$$

where $\boldsymbol{F}_1$ and $\boldsymbol{F}_2$ are the forces distributed on nodes N_1 and N_2, respectively; $\boldsymbol{T}_1$ and $\boldsymbol{T}_2$ are the torques distributed on nodes N_1 and N_2, respectively.

The kinetic energy of the two end nodes is dissipated through deformation and vibration of the fibre, which is considered by using the bond damping forces (the normal component $\boldsymbol{F}_{bd,n}$ and the tangential component $\boldsymbol{F}_{bd,s}$) and moments (the component due to twisting $\boldsymbol{M}_{bd,n}$ and the component due to bending $\boldsymbol{M}_{bd,b}$) between the two nodes of the fibre (Tangri, Guo, and Curtis 2017; Guo et al. 2018):

$$\begin{cases} \boldsymbol{F}_{bd,n} = \beta_b\sqrt{2m_c k_n^b}\boldsymbol{v}_n^b, & \boldsymbol{F}_{bd,s} = \beta_b\sqrt{2m_c k_s^b}\boldsymbol{v}_s^b \\ \mathbf{M}_{bd,t} = \beta_b\sqrt{2J_c k_t^b}\boldsymbol{\omega}_t, & \mathbf{M}_{bd,b} = \beta_b\sqrt{2J_c k_b^b}\boldsymbol{\omega}_b \end{cases} \tag{12}$$

where β_b is the bond damping coefficient and is taken as 0.03, m_c is the mass of the fibre, $\boldsymbol{v}_n^b$ is the relative normal velocity between the two nodes of the fibre, and J_c is the moment of inertia of the end node.

3. Results and discussion

In this section, the DEM model is used to analyse the flow dynamics of the fibre/polymer powder particles and the formation mechanisms of voids in a powder bed. PBF additive manufacturing is a complex multi-scale and multi-physics process that is affected by various environmental factors and processing parameters. The packing parameters that are of vital importance for the quality of the printed parts include the powder size and shape, powder layer thickness, roller spreading velocity, and weight fraction of fibres (Yu, Sing, Chua, Kuo, et al. 2019; Tan, Kiran, and Zhou 2021; Tan et al. 2019). The model is utilised to investigate the effects of packing parameters on the packing quality of the powder bed, which is assessed by two parameters: packing density and surface roughness. The results could help in optimising the packing parameters for achieving a high-quality powder bed.

3.1. Model parameter calibration

The DEM model is calibrated by the static AOR of powder particles, which is usually used to evaluate the flowability of granular materials. The schematic to measure the AOR in the experiment and simulation is demonstrated in Figure 4. The fibres with an average length of 122 μm and a diameter of 11 μm are considered. At the beginning of the experiment, the powder particles were confined in a cylinder with a bottom opening, which rested on a circular plate. Afterwards, the cylinder was lifted slowly so that the powder particles would be deposited onto the circular plate to form a powder pile. The AOR is defined as the angle α between the curved surface of the static powder pile and the horizontal plane. Similar methods to measure the AOR of particles can be found in the reported works (Meier et al. 2019b; Rackl and Hanley 2017; Roessler and Katterfeld 2018).

The material properties used for parameter calibration and DEM packing simulation of glass fibres and PA12 are listed in Table 1. To accelerate the simulation, the Young's modulus of each material is set to be 500 times smaller than the original value to increase the time step. Accordingly, the Hamaker constant of PA12 used in the model is 500 times smaller than the original value (2×10^{-20} J) (Parteli and Pöschel 2016). The surface energy density γ of the materials can be calculated as

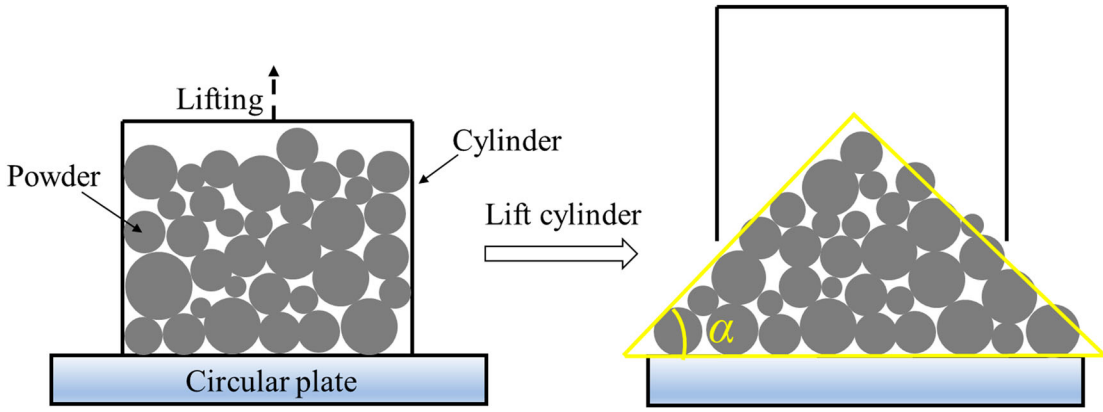

Figure 4. Schematic of measuring the AOR of powder particles.

follows:

$$\gamma = \frac{A}{24\pi D_{\min}^2} \tag{13}$$

where A is the Hamaker constant and $D_{\min}$ is taken as 1.65×10^{-10}m. It is difficult to determine the contact parameters for glass fibres, including the surface energy density, coefficient of restitution, and coefficient of friction. The Hamaker constant of glass fibres is estimated by using that of silica, which is reported to be 6.5×10^{-20} J (Bergström 1997). By considering the reduction of the Young's modulus, the surface energy density is estimated as 0.065 mJ/m^2 according to Equation (13). The coefficient of restitution and the coefficient of friction for glass fibres are estimated in the calibration process to ensure that the AOR of the composite powder particles in the simulation matches the experimental results.

For the contact of two particles with the same material, the contact parameters such as the coefficient of restitution, coefficient of friction, and surface energy density can be straightforwardly adopted. For the contact of two particles with different materials, the surface energy density is taken as zero, and the coefficient of restitution λ and the coefficient of friction μ are calculated as follows:

$$\begin{cases} \lambda = \dfrac{\lambda_1 + \lambda_2}{2} \\ \mu = \min(\mu_1, \mu_2) \end{cases} \tag{14}$$

where λ_1 and λ_2 are the coefficients of restitution for the two contact particles, respectively; μ_1 and μ_2 are the coefficients of friction for the two contact particles, respectively.

To guarantee a stable simulation of the sphere-sphere contact, the estimated time step is given as (Václav Šmilauer and Chareyre 2019):

$$\Delta t = 0.3R_{\min}\sqrt{\frac{\rho}{E}} \tag{15}$$

where $R_{\min}$ is the minimum radius of spherical members that compose the multi-sphere particles and ρ denotes the density. A flexible fibre used in the simulation requires a critical time step as follows (Nan, Wang, and Tang 2015; Guo et al. 2013):

$$\Delta t_b = 0.8165d\sqrt{\frac{\rho}{E}} \tag{16}$$

where d is the diameter of fibres. A time step $\Delta t = 0.25\Delta t_b$ can ensure numerical stability for flexible fibre particles (Nan, Wang, and Tang 2015). Considering the requirements of the time step in Equations (15) and (16), we adopted a time step $\Delta t = 5 \times 10^{-9}$ s for the simulations.

The AOR of the powder particles with different weight fractions of fibres w obtained from the experiment and simulation is given in Figure 5. Both the experiment and simulation results reveal that the AOR increases with the increasing weight fraction of fibres. The increase of the AOR indicates the reduction in the flowability of the composite powder particles, which is critical to the packing quality of the powder bed.

Table 1. Material properties used for the DEM simulation (Parteli and Pöschel 2016; Nan et al. 2018; Bergström 1997; Karuppanan et al. 2014; AZoM 2021).

Parameter	PA12	Glass fibre	Stainless steel 316L
Density ρ (kg/m^3)	1020	2590	7800
Young's modulus E (MPa)	3.9	145.0	386.0
Poisson ratio ν	0.39	0.21	0.30
Coefficient of restitution λ	0.50	0.65	0.64
Coefficient of friction μ	0.50	0.60	0.60
Surface energy density γ (mJ/m^2)	0.02	0.065	\
Acceleration of gravity g (m/s^2)	9.8	9.8	9.8

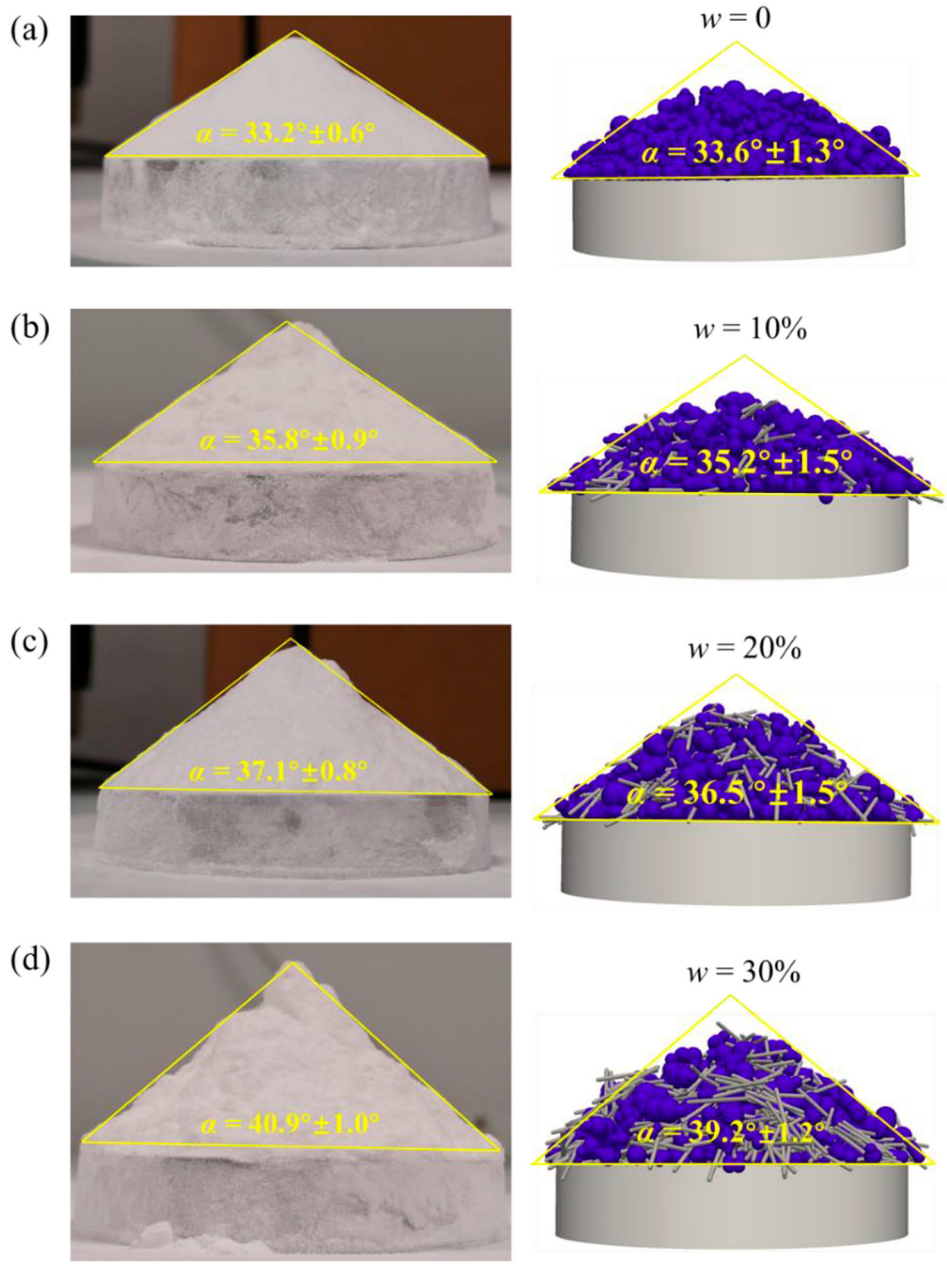

Figure 5. AOR of PA12 and composite powder particles with different weight fractions of fibres: (a) $w = 0$, (b) $w = 10\%$, (c) $w = 20\%$, and (d) $w = 30\%$.

Consequently, the curved surface of the powder pile becomes coarser as the weight fraction of the fibres increases. The simulation and experiment results agree well on the AOR of powder particles.

3.2. Flow dynamics of fibre/polymer composite powder in the packing process

A roller-type packing system composed of a counter-rotating roller and a substrate is considered in the model, as illustrated in Figure 6. A roller with a radius $R = 10$ mm moves along the x direction and simultaneously rotates in the counter-clockwise direction. Periodic boundary conditions are applied to the y direction at $y = 0$ and $y = 0.65$ mm. Initially, a cloud of fibre/PA12 composite powder particles with a packing density of 0.45, which are enclosed in a rectangular box, is dropped onto the substrate under the gravitational force. As a pile of fibre/PA12 powder particles is formed on the substrate, the roller with a translational velocity v and an angular velocity $\omega = v/R$ spreads the composite powder particles along the x direction. After being spread by the roller, the powder particles are deposited onto the substrate and form a static powder

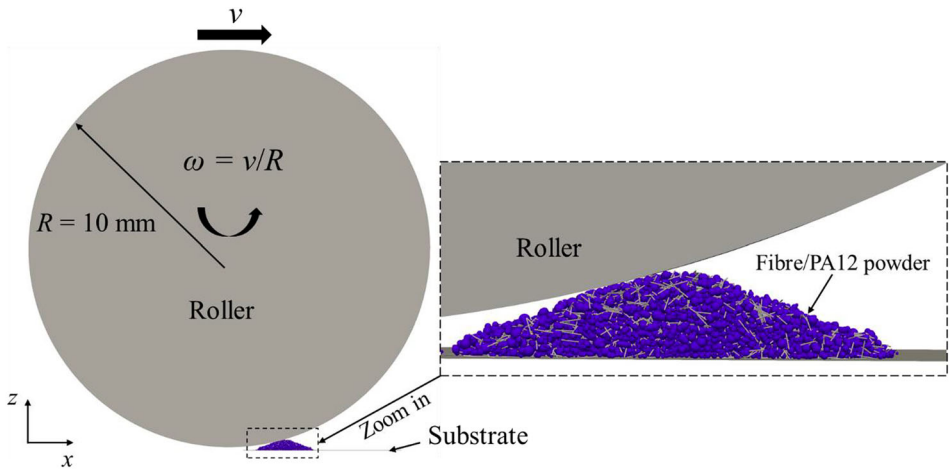

Figure 6. Schematic of the roller-type spreading system in the simulation.

bed. The material properties used for simulating the packing process of glass fibres and PA12 powder particles are listed in Table 1. Stainless steel 316L is taken to be the material of the roller and substrate.

The flow dynamic behaviours of the composite powder particles in the packing process play an important role in the packing quality of the powder bed. A snapshot of the packing process is demonstrated in Figure 7. The roller spreading velocity v and the powder layer thickness H are 0.1 m/s and 150 μm, respectively. The composite powder particles with $w =$ 20% consist of 4500 PA12 powder particles and 4561 glass fibres. The size of the PA12 powder follows the particle size distribution in Figure 2(b). In the following simulations, the fibres with a diameter of 8 μm and a length evenly ranging from 80 μm to 120 μm are used. Figure 7(a) shows a three-dimensional (3D) view of the packing process in which a pile of fibre/polymer powder particles is spread by a roller on the substrate. In general, the distribution of powder particles can be divided into two regions, i.e. the static powder bed and dynamic powder pile, by the narrowest gap between the roller and the substrate. In the dynamic powder pile, the powder particles with large velocity magnitudes are mainly distributed on the free surface and the contact surface with the roller, which are caused by the gravitational force and the contact interaction with the roller, respectively. The powder particles near the static substrate possess low velocity magnitudes. From the top view of the packing process in Figure 7(b), the particle velocity magnitude generally decreases from the free surface to the static powder bed.

Figure 7(c)–(f) shows the x–z cross section of the powder bed and powder pile clipped between $y_0 = 325$ μm and $y_1 = 500$ μm. The velocity magnitude and velocity vector of the composite powder particles are shown in Figure 7(c) and (e), respectively. After the PA12 powder particles are removed, the powder pile contains only fibres, as shown in Figure 7(d). On the free surface of the powder pile, powder particles tend to slide down because of gravity. In the dynamic powder pile, most of the powder particles are dragged by the roller and thus move in the x direction. With the gap between the roller and the substrate being narrower, the powder particles gradually have smaller velocity magnitudes. There exists a downward velocity in the narrowest gap, which enables the deposition of powder particles onto the substrate. Figure 7(f) shows that there exists a strongly inhomogeneous distribution of contact force in the powder particles due to the formation of force chains. The force chains that commonly exist in granular materials (Parteli and Pöschel 2016) lead to the load concentration on a small number of powder particles.

Voids in a powder bed are detrimental to the packing density and surface morphology. As shown in Figure 8, the numerical model is capable of predicting the formation process of voids in the powder bed. Figure 8 (a)–(e) shows the evolutions of the powder velocity and the contact force in the regions enclosed by the dashed rectangle in Figure 7(c). In particular, Figure 8 (a) shows a stable powder flow in which the powder particles have their velocities in the moving direction of the roller. As the powder particles are spread by the roller, as shown in Figure 8(b), strong force chains may be newly developed in a few powder particles near the narrowest gap between the roller and the substrate. The newly developed force chains may hinder the movement of the roller and have a strong interaction with the roller. Hence, a sharp peak can be observed at $t = 32.9$ ms in the evolution of the contact force on the roller, as shown in Figure 8(f). Because of the strong force

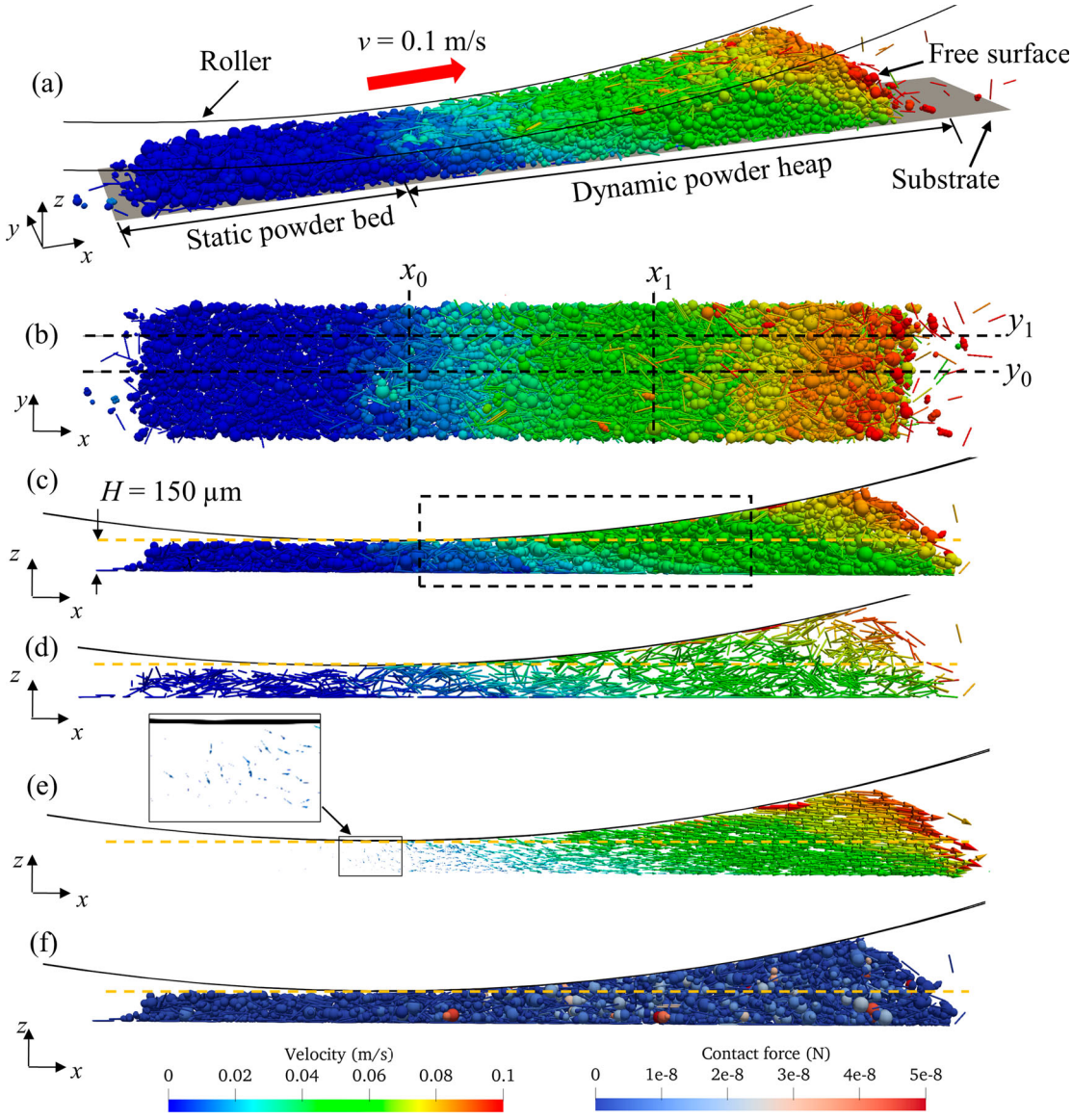

Figure 7. Snapshot of the packing process of fibre/polymer powder particles: (a) 3D view of the powder velocity, (b) top view of the velocity field, (c) x–z cross section of the velocity field, (d) x–z cross section of the powder pile after removing the PA12 powder particles, (e) x–z cross section of the velocity vector, and (f) x–z cross section of the contact force field.

interaction with the roller, the powder particles would undergo a strong dragging effect by the roller. Consequently, a void is gradually developed as shown in Figure 8(c).

To better observe the formation process of the void in Figure 8(b) and (c), snapshots of the top view of the powder bed are shown in Figure 9. The region of the top view is confined between x_0 and x_1, as shown in Figure 7(b). At $t = 32.9$ ms, several particles in the dashed circle are spread by the roller and possess large velocities. With the movement of these particles, their positions and orientations are rearranged, and they start to be deposited onto the substrate. After $t = 33.5$ ms, a void starts to gradually develop. The particles that were in the void position have been dragged forward along the spreading direction by the roller. A similar void formation process is repeated in Figure 8(c) and (d). After the powder particles are deposited onto the substrate and form a static powder bed, two voids are finally developed, as shown in Figure 8(e).

3.3. Effects of packing parameters on the packing quality of the powder bed

The numerical model is used to investigate the effects of packing parameters on the packing quality of the powder bed, which is quantified by two parameters: the packing density and surface roughness. The

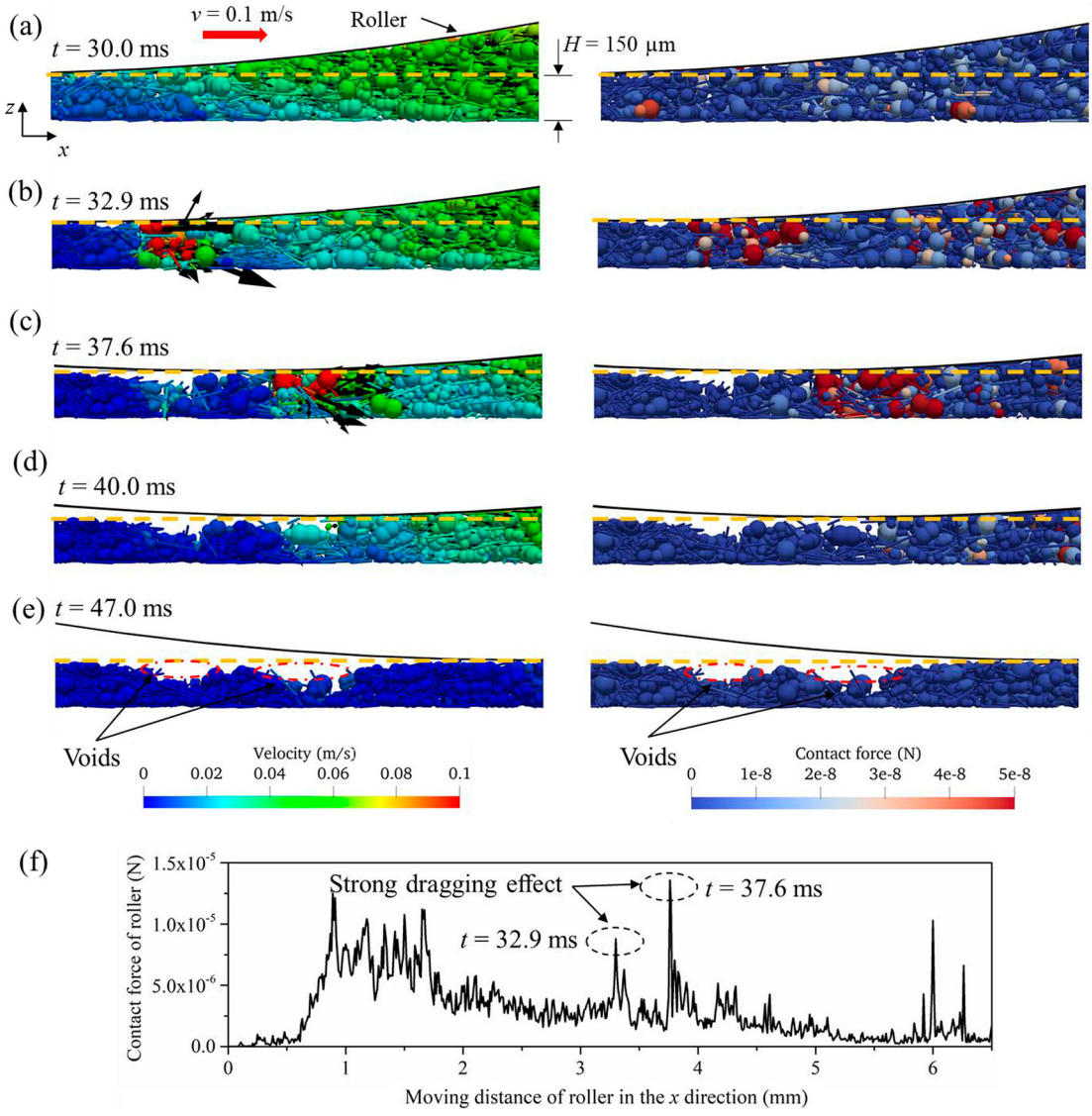

Figure 8. Formation process of voids in the packing process of fibre/polymer powder particles: (a) $t = 30.0$ ms, (b) $t = 32.9$ ms, (c) $t = 37.6$ ms, (d) $t = 40.0$ ms, and (e) $t = 47.0$ ms (the snapshots are for the regions enclosed by the dashed rectangle in Figure 7(c)). (f) Evolution of the contact force applied to the roller with the roller moving distance in the x direction.

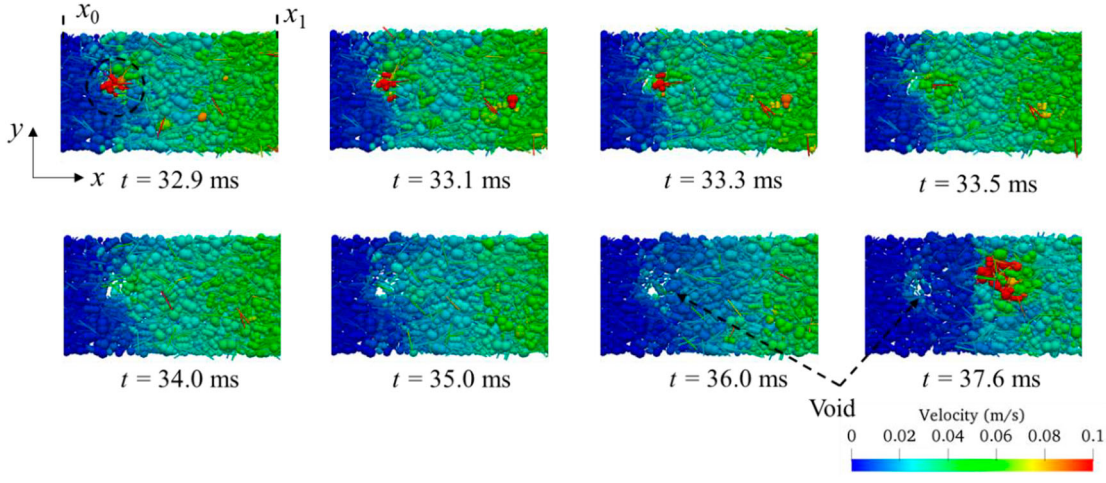

Figure 9. Snapshots of the formation process of the void in the packing process of fibre/polymer powder particles.

packing density φ is defined as

$$\varphi = \frac{V_p}{LWH} \tag{17}$$

where V_p is the volume of PA12 and fibre powder particles; L, W, and H are the length, width, and thickness of the powder bed, respectively. A larger packing density indicates a more compact powder bed, which has positive effects on the minimisation of porosity in the printed composites.

The surface roughness ε is used to evaluate the surface smoothness of the powder bed, which is defined as the standard deviation of the height profile of the powder bed:

$$\varepsilon = \sqrt{\frac{\sum_{i=1}^{N}(h_i - h_a)^2}{N-1}} \tag{18}$$

where N is the number of points, h_i is the height of the powder bed at one point, and h_a is the average value of the height profile. To calculate the height profile, a ray-tracing method is adopted to capture the top surface of the powder bed (Haeri et al. 2017; Meier et al. 2019a). At any point, this top surface is determined at the highest intersection position of the ray and powder particles. In this study, the height profile along the spreading direction (the x direction) is the projection of the powder bed clipped between $y = y_0$ and $y = y_1$ onto the x–z plane. The surface roughness is obtained from the height profiles of the powder bed along the spreading direction.

To evaluate the packing microstructure, the coordination number that is defined as the average contact number of the considered particle is calculated as

$$N_c = \frac{2C}{N} \tag{19}$$

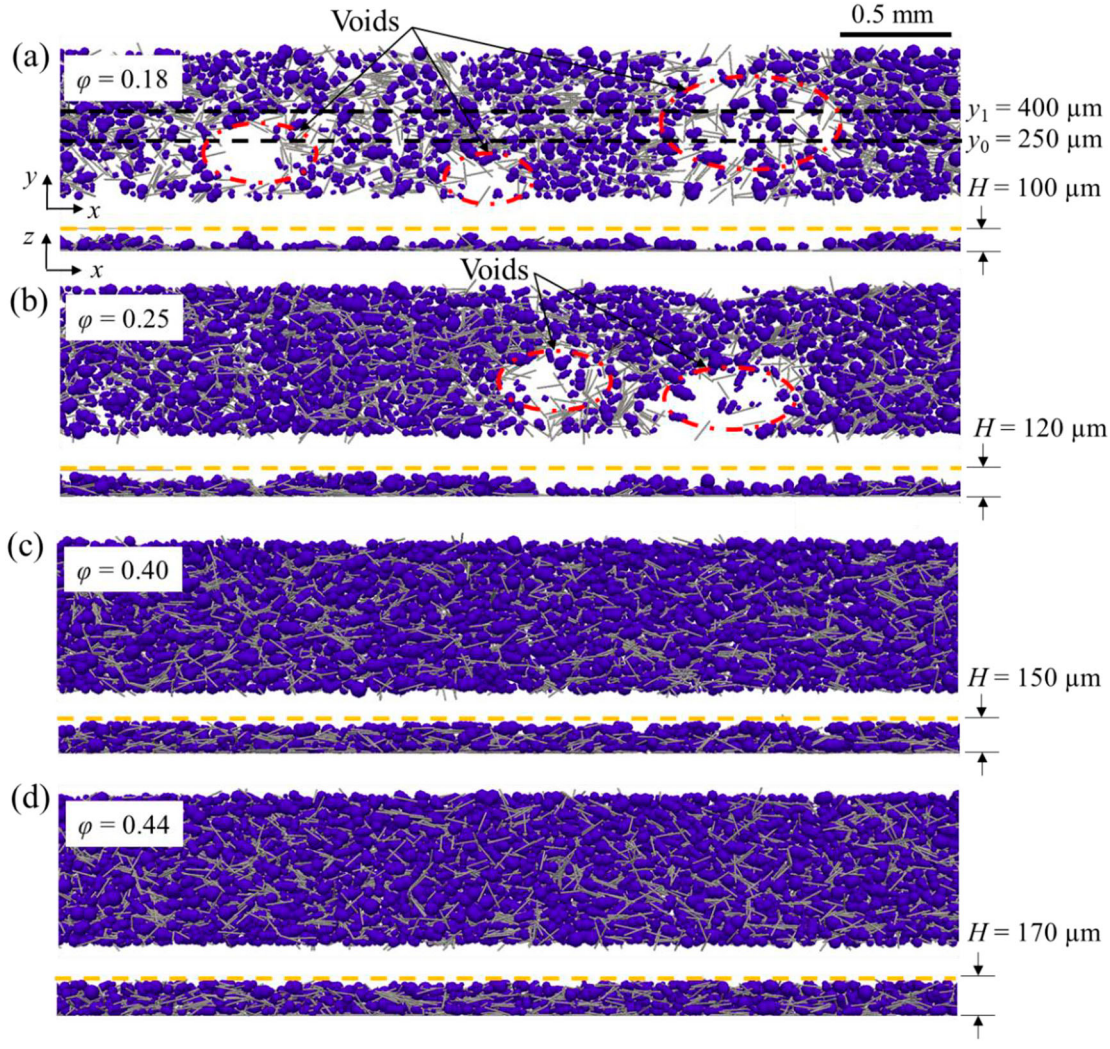

Figure 10. Powder beds with different powder layer thicknesses ($v = 0.1$ m/s and $w = 20\%$): (a) $H = 100$ μm, (b) $H = 120$ μm, (c) $H = 150$ μm, and (d) $H = 170$ μm. The orange dash line denotes the bottom position of the roller.

where C is the total contact number and N is the number of particles. The multi-sphere polymer particle including several spherical members is regarded as one particle in the calculation. The contact number of a multi-sphere particle is the summation of the contact number of each spherical member. The contact between the spherical members within the multi-sphere particle is not considered. The cohesive interaction of two nodes in one fibre particle is not counted into the total contact number. Considering the above assumptions, we can obtain the total contact number, and calculate the coordination number.

3.3.1. Powder layer thickness

The powder layer thickness is defined as the narrowest gap between the roller and the substrate and is a crucial parameter that influences the flow behaviour of powder particles in the packing process. Figure 10 shows the powder beds of PA12 and fibres with different powder layer thicknesses ($H = 100$, 120, 150, and 170 μm). In this case, the roller spreading velocity and the weight fraction of fibres in the composite powder particles are fixed to be 0.1 m/s and 20%, respectively. The top view (the x–y plane) of the powder bed and the x–z cross section of the powder bed clipped between $y_0 = 250$ μm and $y_1 = 400$ μm are shown in Figure 10(a). With the increase of the powder layer thickness, the powder bed has fewer voids and becomes more compact. The packing density and surface roughness of the powder beds with different powder layer thicknesses are plotted in Figure 11(a). The increase of the powder layer thickness can improve the packing quality of the powder bed as indicated by the larger packing density and lower surface roughness, which is consistent with the conclusions reported by Haeri et al. (2017). As the powder layer thickness becomes larger than 170 μm, the improvement in the packing quality due to the variation of the powder layer thickness is insignificant. Although a large layer thickness can improve the packing quality of the bed, it may result in the lack of fusion in the powder melting process and reduce the dimensional accuracy of the printed parts. The height profiles in the x–z cross section of powder beds with different powder layer thicknesses are plotted in Figure 11(b). The increase of the powder layer thickness can lead to an increase in the average height of the powder bed. Moreover, the height profile of the powder bed with a thicker powder layer has a smaller fluctuation along the spreading direction, which indicates a smoother powder bed.

The voids in a powder bed with a thin powder layer thickness were mainly ascribed to the jamming

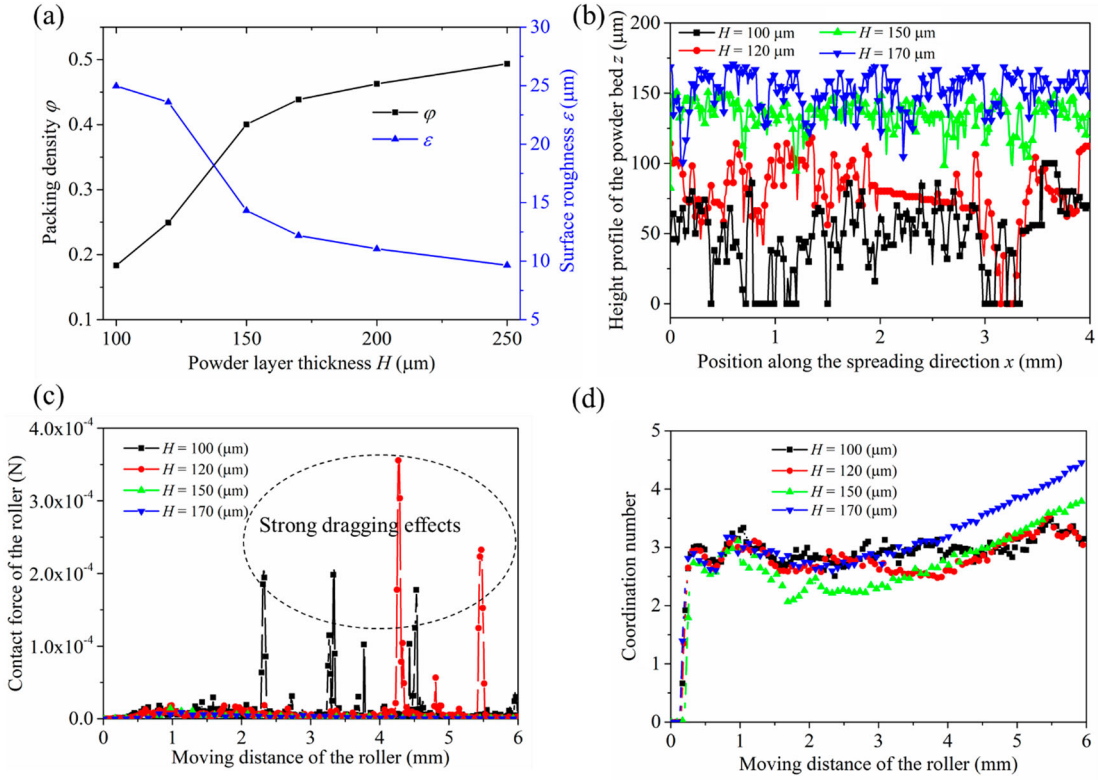

Figure 11. Effects of the powder layer thickness on (a) packing density and surface roughness, and (b) height profile of the powder bed. Evolutions of (c) the contact force on the roller and (d) the coordination number in the packing process with different powder layer thicknesses.

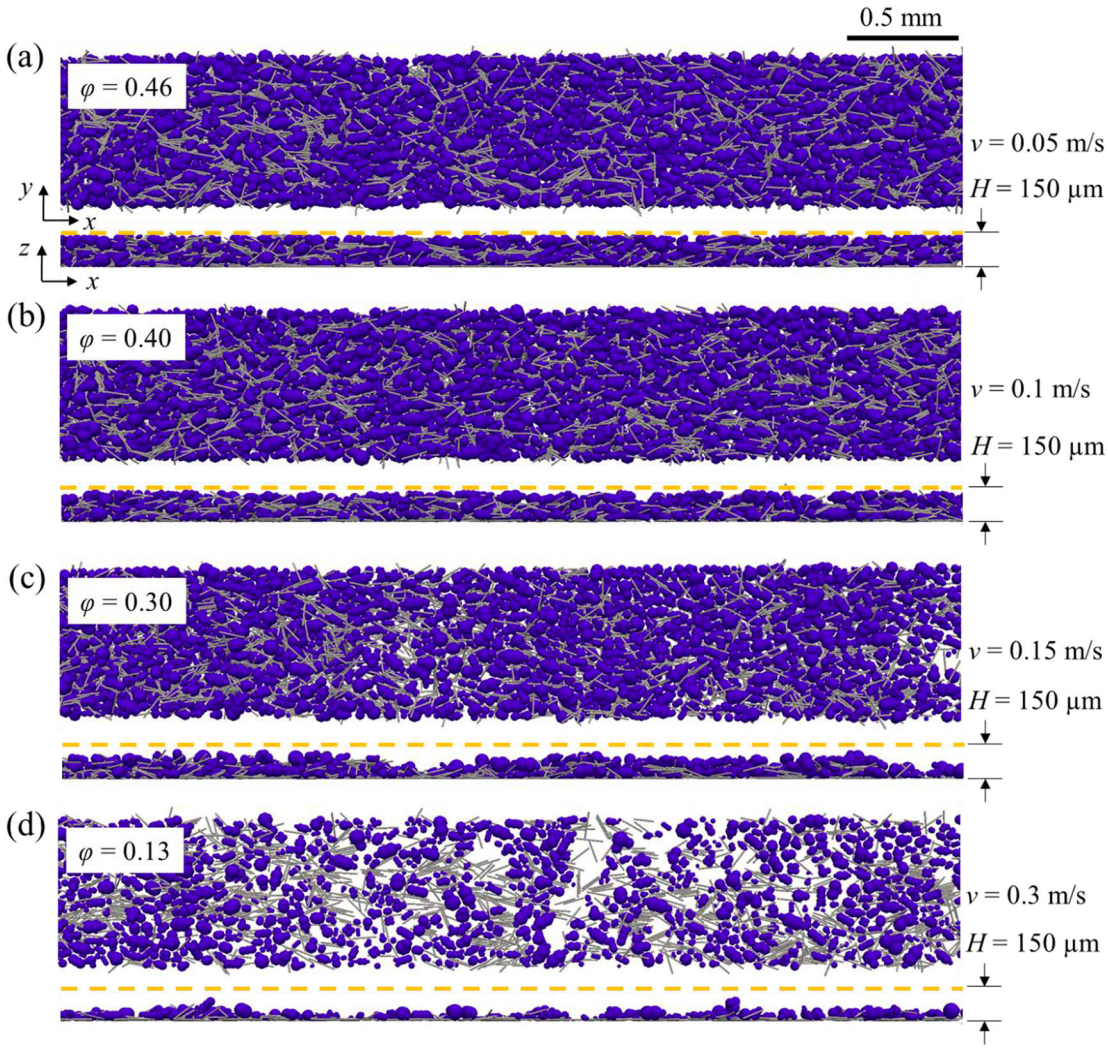

Figure 12. Powder beds with different roller spreading velocities ($H = 150$ μm and $w = 20\%$): (a) $v = 0.05$ m/s, (b) $v = 0.1$ m/s, (c) $v = 0.15$ m/s, and (d) $v = 0.3$ m/s.

phenomenon in the packing process by Nan et al. (2018), and they found that the total jamming probability decreased sharply with the increase of the gap between the blade spreader and the substrate. With the decrease of the powder layer thickness, the powder particles have less space to rearrange in the gap between the roller and the substrate. Consequently, when being pushed by the roller, more powder particles may experience strong contact interaction forces, thus leading to a higher chance of the emergence of strong force chains more easily. The jamming may be caused by these strong force chains, especially for the non-spherical powder particles with large sizes. Figure 11(c) illustrates the evolution of the contact force applied to the roller for powder beds with different powder layer thicknesses in the packing process. A decrease in the powder layer thickness leads to a significant increase in the contact force of the roller. A few peaks are found in the evolutions of the contact forces at $H = 100$ and 120 μm, which are one order of magnitude larger than those at $H = 150$ and 170 μm. These peaks of the contact force imply a strong interaction between the powder particles and the roller. Consequently, these powder particles are strongly dragged forward by the roller, which leads to the emergence of voids in the powder bed.

Figure 11(d) shows the evolutions of the coordination number in the packing process for powder beds with different powder layer thicknesses. Initially, the coordination number is zero because no contact exists in the loose powder pile. As the powder pile drops onto the substrate because of gravity, the coordination number has an abrupt increase. As the roller starts to spread powder particles onto the substrate, the coordination number experiences a fluctuation. The packing process becomes stable as the roller moves around 2 mm. Consequently, the coordination number tends to increase because more powder particles are deposited onto the

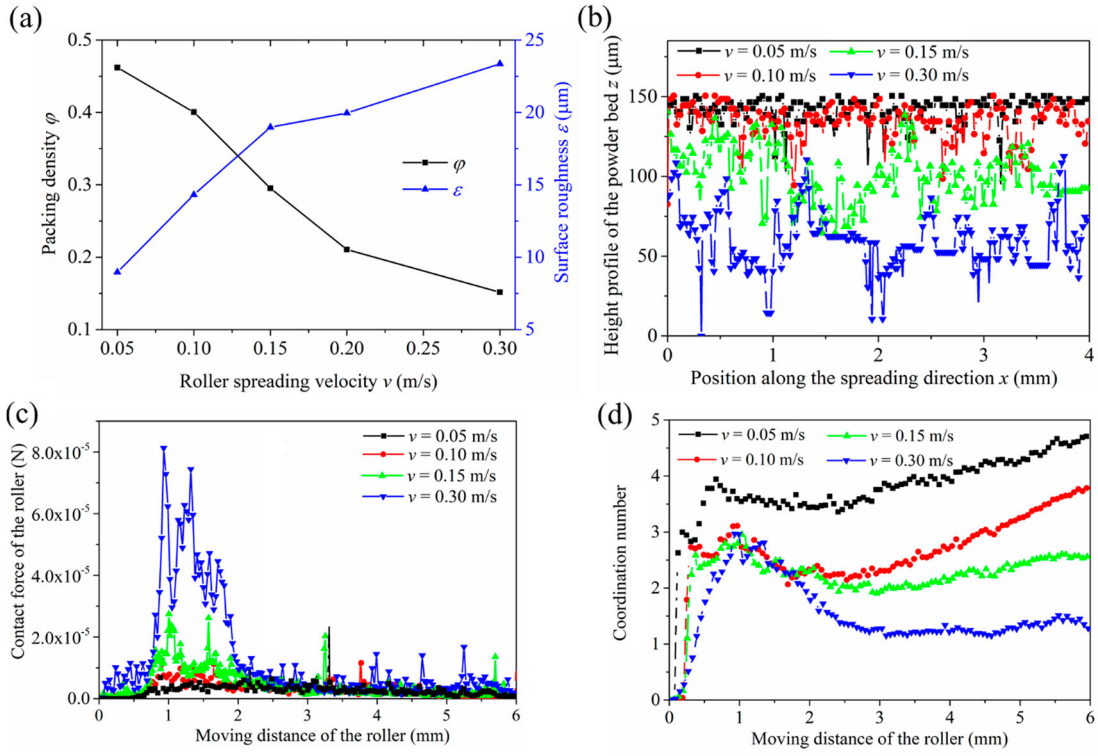

Figure 13. Effects of the roller spreading velocity on (a) packing density and surface roughness, and (b) height profile of the powder bed. Evolutions of (c) the contact force on the roller and (d) the coordination number in the packing process with different spreading velocities.

substrate and form a static powder bed. In general, the coordination number increases faster for the packing processes of powder beds with larger powder layer thicknesses.

3.3.2. Roller spreading velocity

Figure 12 demonstrates the powder beds with different roller spreading velocities. The powder layer thickness and the weight fraction of fibres in the composite powder particles are taken as 150 μm and 20%, respectively. As the spreading velocity increases, more voids are found in the powder bed. Particularly, at $v = 0.3$ m/s, the powder distribution is extremely sparse, and a discontinuous thin powder bed is observed. The packing density and surface roughness of the powder bed at different spreading velocities are shown in Figure 13(a). The increase of the spreading velocity reduces the packing density and increases the surface roughness, indicating a poor packing quality of the powder bed. Chen et al. (2020) reported similar conclusions from the experiment and simulation results for the packing process of metal powder particles, and Parteli and Pöschel (2016) also found that the increase of the spreading velocity led to a rougher powder bed. Even though a small spreading velocity can be beneficial to the packing quality of the powder bed, the printing efficiency is lowered. A balance between the packing quality and printing efficiency should be considered for the setting of the roller spreading velocity. The height profiles along the spreading direction of the powder bed at different spreading velocities are plotted in Figure 13(b). The increase in the spreading velocity leads to a decrease in the average height and a rougher top surface of the powder bed.

Figure 13(c) plots the evolutions of the contact force applied to the roller in the packing process at different spreading velocities. Large contact forces are observed when the moving distance of the roller is between 0.5 and 2 mm. During this period, the roller starts to spread the static powder pile onto the substrate so that a faster roller is subjected to stronger force interactions. After the spreading process becomes stable (the moving distance is larger than around 2 mm), the spreading velocity has no obvious effect on the contact force of the roller except that a few more force peaks occur for $v = 0.3$ m/s. Figure 13(d) shows the evolution of the coordination number in the packing process with different spreading velocities. An increase in the spreading velocity results in a decrease in the coordination number. A low coordination number in the packing process of powder beds with high spreading velocities results in insufficient powder contact in the

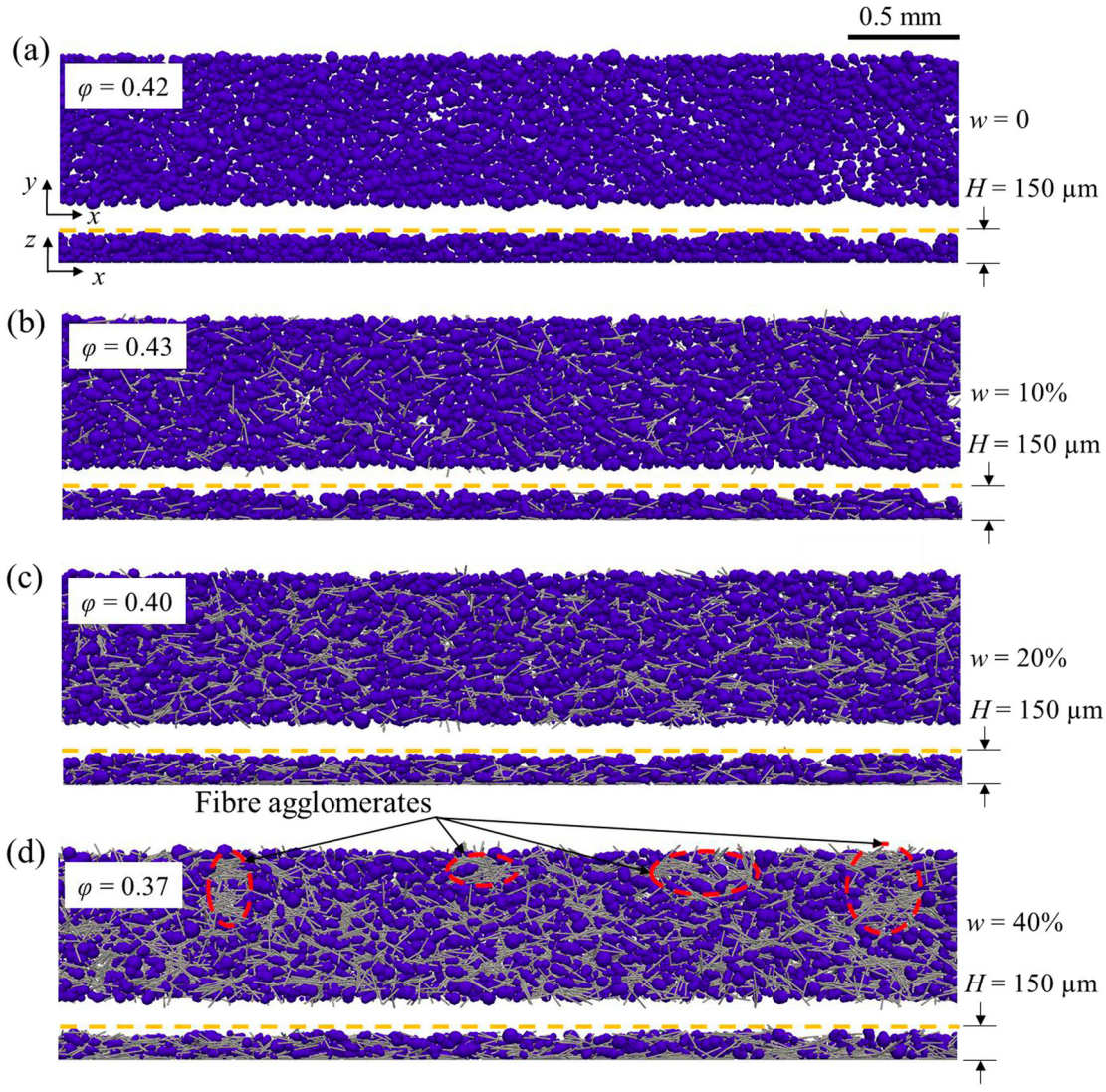

Figure 14. Powder beds with different weight fractions of fibres ($H = 150$ μm and $v = 0.1$ m/s): (a) $w = 0$, (b) $w = 10\%$, (c) $w = 20\%$, and (d) $w = 40\%$.

packing process, which would degrade the packing quality of the powder bed.

3.3.3. Weight fraction of fibres

The powder beds with different weight fractions of fibres are shown in Figure 14. The powder layer thickness ($H =$ 150 μm) and roller spreading velocity ($v = 0.1$ m/s) are kept constant. The variation of the packing density and surface roughness of the powder bed with different weight fractions of fibres is demonstrated in Figure 15 (a). The packing density of the powder bed with a small number of fibres ($w = 5\%$ and 10%) increases slightly as compared with that of the PA12 powder bed. Meanwhile, the surface roughness reduces with the increase of the weight fraction of fibres. The packing quality is improved when a few fibres are mixed with PA12 powder particles because the fibres can fill the voids among PA12 powder particles due to its smaller volume. When $w > 10\%$, the surface roughness has no noticeable variation tendency, while the packing density reduces with an increasing weight fraction of the fibres. This change can be attributed to the reduction of flowability for fibre/PA12 composite powder particles and the agglomeration of the fibres. As shown in Figure 5, the increase in the weight fraction of fibres contributes to a higher AOR for the composite powder particles, which indicates the reduction of the powder flowability. Moreover, fibres with small sizes tend to agglomerate in the packing process because of the cohesive force, as shown in Figure 14(d).

The height profiles of the powder beds with different weight fractions of fibres are shown in Figure 15(b). In Figure 15(c), the contact forces on the roller demonstrate a similar evolution trend for the powder beds

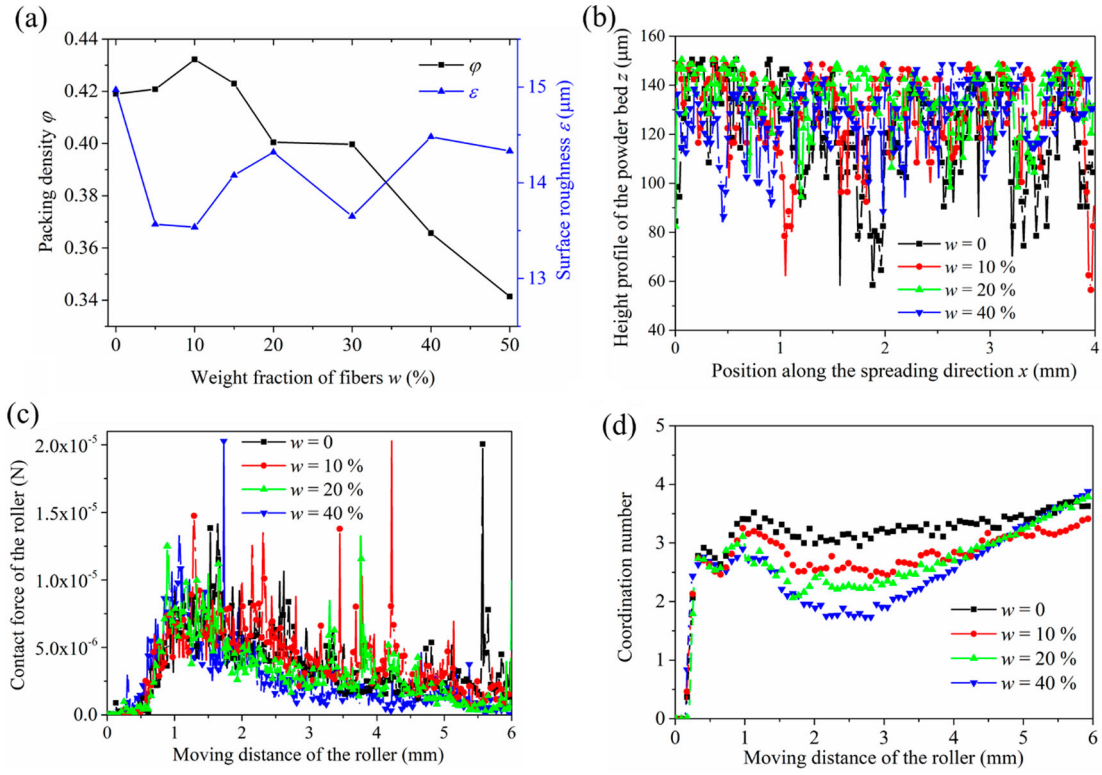

Figure 15. Effects of the weight fraction of fibres on (a) packing density and surface roughness, and (b) height profile of the powder bed. Evolutions of (c) the contact force on the roller and (d) the coordination number in the packing process with different weight fractions of fibres.

with different weight fractions of fibres. Figure 15(d) shows the evolutions of the coordination number in the packing process for the powder beds with different weight fractions of fibres. When the moving distance of the roller is between 1 and 4 mm, the coordination number generally reduces as the weight fraction of fibres increases. After the roller moves around 4 mm, the coordination number increases as more powder particles are deposited onto the substrate to form a static powder bed. During this period, the weight fraction of fibres has no noticeable effect on the coordination number.

4. Conclusions

A DEM model has been developed for simulating the packing process of fibre/polymer composite powder particles for PBF additive manufacturing. In the numerical model, polymer powder particles and fibres are represented by multi-sphere particles and individual cylinders with round ends, respectively. The static AOR of composite powder particles measured in the experiment is used to calibrate the parameters used in the model. The model provides an efficient and feasible way to predict the packing characteristics of powder beds. In this study, the model has been employed to investigate the flow dynamics of composite powder particles and study the effects of packing parameters on the packing quality of the powder bed.

The distribution of the particle contact force is strongly inhomogeneous, and the emergence of new strong force chains near the gap between the roller and the substrate may lead to the formation of voids in the powder bed. The increase of the powder layer thickness is beneficial to the increase in the packing density and the decrease in the surface roughness of the powder bed due to the reduction of strong dragging effects. The high roller spreading velocity leads to insufficient contact interactions among powder particles in the packing process, which reduces the packing quality of the powder bed. A small number of fibres mixed with polymer powder particles are in favour of the packing quality, but a further increase in the fibre number lowers it because of the reduction of powder flowability and agglomeration of fibres.

Acknowledgments

This research was conducted in collaboration with HP Inc. and supported by Nanyang Technological University and the Singapore Government through the Industry Alignment Fund-Industry Collaboration Projects Grant.

Disclosure statement

No potential conflict of interest was reported by the author(s).

Funding

This research was supported by the Industry Alignment Fund-Industry Collaboration Projects Grant from HP Inc. and the Singapore Government.

Notes on contributors

Pengfei Tan is a Research Fellow in HP-NTU Digital Manufacturing Corporate Lab, School of Mechanical and Aerospace Engineering, Nanyang Technological University, Singapore.

Fei Shen is an Associate Professor in Department of Mechanics, School of Mechanical Engineering, Tianjin University, China.

Wei Shian Tey is a PhD candidate in HP-NTU Digital Manufacturing Corporate Lab, School of Mechanical and Aerospace Engineering, Nanyang Technological University, Singapore.

Kun Zhou is an Associate Professor in School of Mechanical and Aerospace Engineering, Nanyang Technological University, Singapore.

ORCID

Kun Zhou http://orcid.org/0000-0001-7660-2911

References

Arai, S., S. Tsunoda, A. Yamaguchi, and T. Ougizawa. 2018. "Effects of Short-Glass-Fiber Content on Material and Part Properties of Poly(Butylene Terephthalate) Processed by Selective Laser Sintering." *Additive Manufacturing* 21: 683–693. doi:10.1016/j.addma.2018.04.019.

AZoM. 2021. "E-Glass Fibre." In. https://www.azom.com/properties.aspx?ArticleID=764: AZoM.

Bergström, L. 1997. "Hamaker Constants of Inorganic Materials." *Advances in Colloid and Interface Science* 70: 125–169.

Bourrier, F., F. Kneib, B. Chareyre, and T. Fourcaud. 2013. "Discrete Modeling of Granular Soils Reinforcement by Plant Roots." *Ecological Engineering* 61: 646–657. doi:10.1016/j.ecoleng.2013.05.002.

Cai, C., W. S. Tey, J. Chen, W. Zhu, X. Liu, T. Liu, L. Zhao, and K. Zhou. 2021. "Comparative Study on 3D Printing of Polyamide 12 by Selective Laser Sintering and Multi jet Fusion." *Journal of Materials Processing Technology* 288,.

Chen, H., Y. Chen, Y. Liu, Q. Wei, Y. Shi, and W. Yan. 2020. "Packing Quality of Powder Layer During Counter-Rolling-Type Powder Spreading Process in Additive Manufacturing." *International Journal of Machine Tools and Manufacture* 153, doi:10.1016/j.ijmachtools.2020.103553.

Chen, H., Q. Wei, Y. Zhang, F. Chen, Y. Shi, and W. Yan. 2019. "Powder-spreading Mechanisms in Powder-bed-Based Additive Manufacturing: Experiments and Computational Modeling." *Acta Materialia* 179: 158–171. doi:10.1016/j.actamat.2019.08.030.

Cundall, P. A., and O. D. Strack. 1979. "A Discrete Numerical Model for Granular Assemblies." *Géotechnique* 29 (1): 47–65.

Derjaguin, B. V., V. M. Muller, and Y. P. Toporov. 1975. "Effect of Contact Deformations on the Adhesion of Particles." *Journal of Colloid and Interface Science* 53 (2): 314–326.

Derksen, J. J. 2020. "Particle-resolved Simulations of Liquid Fluidization of Rigid and Flexible Fibers." *Acta Mechanica* 231 (12): 5193–5203. doi:10.1007/s00707-020-02832-2.

Effeindzourou, A., B. Chareyre, K. Thoeni, A. Giacomini, and F. Kneib. 2016. "Modelling of Deformable Structures in the General Framework of the Discrete Element Method." *Geotextiles and Geomembranes* 44 (2): 143–156. doi:10.1016/j.geotexmem.2015.07.015.

Escano, L. I., N. D. Parab, L. Xiong, Q. Guo, C. Zhao, K. Fezzaa, W. Everhart, T. Sun, and L. Chen. 2018. "Revealing Particle-Scale Powder Spreading Dynamics in Powder-bed-Based Additive Manufacturing Process by High-Speed x-Ray Imaging." *Scientific Report* 8 (1): 15079. doi:10.1038/s41598-018-33376-0.

Goh, G. D., Y. L. Yap, S. Agarwala, and W. Y. Yeong. 2019. "Recent Progress in Additive Manufacturing of Fiber Reinforced Polymer Composite." *Advanced Materials Technologies* 4 (1): 1800271. doi:10.1002/admt.201800271.

Gu, D., M. Xia, and D. Dai. 2019. "On the Role of Powder Flow Behavior in Fluid Thermodynamics and Laser Processability of Ni-Based Composites by Selective Laser Melting." *International Journal of Machine Tools and Manufacture* 137: 67–78. doi:10.1016/j.ijmachtools.2018.10.006.

Guo, Y., C. Wassgren, J. S. Curtis, and D. Xu. 2018. "A Bonded Sphero-Cylinder Model for the Discrete Element Simulation of Elasto-Plastic Fibers." *Chemical Engineering Science* 175: 118–129. doi:10.1016/j.ces.2017.09.029.

Guo, Y., C. Wassgren, B. Hancock, W. Ketterhagen, and J. Curtis. 2013. "Validation and Time Step Determination of Discrete Element Modeling of Flexible Fibers." *Powder Technology* 249: 386–395. doi:10.1016/j.powtec.2013.09.007.

Haeri, S. 2017. "Optimisation of Blade Type Spreaders for Powder bed Preparation in Additive Manufacturing Using DEM Simulations." *Powder Technology* 321: 94–104. doi:10.1016/j.powtec.2017.08.011.

Haeri, S., Y. Wang, O. Ghita, and J. Sun. 2017. "Discrete Element Simulation and Experimental Study of Powder Spreading Process in Additive Manufacturing." *Powder Technology* 306: 45–54. doi:10.1016/j.powtec.2016.11.002.

Jansson, A., and L. Pejryd. 2016. "Characterisation of Carbon Fibre-Reinforced Polyamide Manufactured by Selective Laser Sintering." *Additive Manufacturing* 9: 7–13. doi:10.1016/j.addma.2015.12.003.

Karuppanan, S., A. N. Mengal, S. Karuppanan, A. A. Wahab, Z. A. Abdul Karim, M. Ovinis, and A. Tesfamichael Baheta. 2014. "Structural Analysis of Basalt Fiber Reinforced Plastic Wind Turbine Blade." *MATEC Web of Conferences* 13), doi:10.1051/matecconf/20141304019.

Kathavate, V. S., D. N. Pawar, and A. S. Adkine. 2019. "Micromechanics-based Approach for the Effective Estimation of the Elastic Properties of Fiber-Reinforced Polymer Matrix Composite." *Journal of Micromechanics and Molecular Physics* 04 (03), doi:10.1142/s242491301950005x.

Kunhappan, D., B. Harthong, B. Chareyre, G. Balarac, and P. J. J. Dumont. 2017. "Numerical Modeling of High Aspect Ratio Flexible Fibers in Inertial Flows." *Physics of Fluids* 29 (9), doi:10.1063/1.5001514.

Kuo, C. N., C. K. Chua, P. C. Peng, Y. W. Chen, S. L. Sing, S. Huang, and Y. L. Su. 2020. "Microstructure Evolution and Mechanical Property Response via 3D Printing Parameter Development of Al–Sc Alloy." *Virtual and Physical Prototyping* 15 (1): 120–129. doi:10.1080/17452759.2019.1698967.

Meier, C., R. Weissbach, J. Weinberg, W. A. Wall, and A. J. Hart. 2019a. "Critical Influences of Particle Size and Adhesion on the Powder Layer Uniformity in Metal Additive Manufacturing." *Journal of Materials Processing Technology* 266: 484–501. doi:10.1016/j.jmatprotec.2018.10.037.

Meier, C., R. Weissbach, J. Weinberg, W. A. Wall, and A. J. Hart. 2019b. "Modeling and Characterization of Cohesion in Fine Metal Powders with a Focus on Additive Manufacturing Process Simulations." *Powder Technology* 343: 855–866. doi:10.1016/j.powtec.2018.11.072.

Modenese, C. 2013. "Numerical Study of the Mechanical Properties of Lunar Soil by the Discrete Element Method." PhD diss., St Anne's College, Oxford.

Nan, W., M. Pasha, T. Bonakdar, A. Lopez, U. Zafar, S. Nadimi, and M. Ghadiri. 2018. "Jamming During Particle Spreading in Additive Manufacturing." *Powder Technology* 338: 253–262. doi:10.1016/j.powtec.2018.07.030.

Nan, W., M. Pasha, and M. Ghadiri. 2020. "Numerical Simulation of Particle Flow and Segregation During Roller Spreading Process in Additive Manufacturing." *Powder Technology* 364: 811–821. doi:10.1016/j.powtec.2019.12.023.

Nan, W., Y. Wang, and H. Tang. 2015. "A Viscoelastic Model for Flexible Fibers with Material Damping." *Powder Technology* 276: 175–182. doi:10.1016/j.powtec.2015.02.037.

Nie, X., Z. Chen, Y. Qi, H. Zhang, C. Zhang, Z. Xiao, and H. Zhu. 2020. "Effect of Defocusing Distance on Laser Powder bed Fusion of High Strength Al–Cu–Mg–Mn Alloy." *Virtual and Physical Prototyping* 15 (3): 325–339. doi:10.1080/17452759.2020.1760895.

Parandoush, P., and D. Lin. 2017. "A Review on Additive Manufacturing of Polymer-Fiber Composites." *Composite Structures* 182: 36–53. doi:10.1016/j.compstruct.2017.08.088.

Parteli, E. J. R., and T. Pöschel. 2016. "Particle-based Simulation of Powder Application in Additive Manufacturing." *Powder Technology* 288: 96–102. doi:10.1016/j.powtec.2015.10.035.

Rackl, M., and K. J. Hanley. 2017. "A Methodical Calibration Procedure for Discrete Element Models." *Powder Technology* 307: 73–83. doi:10.1016/j.powtec.2016.11.048.

Roessler, T., and A. Katterfeld. 2018. "Scaling of the Angle of Repose Test and its Influence on the Calibration of DEM Parameters Using Upscaled Particles." *Powder Technology* 330: 58–66. doi:10.1016/j.powtec.2018.01.044.

Salazar, A., A. Rico, J. Rodríguez, J. Segurado Escudero, R. Seltzer, and F. Martin de la Escalera Cutillas. 2014. "Fatigue Crack Growth of SLS Polyamide 12: Effect of Reinforcement and Temperature." *Composites Part B: Engineering* 59: 285–292. doi:10.1016/j.compositesb.2013.12.017.

Schiochet Nasato, D., and T. Pöschel. 2020. "Influence of Particle Shape in Additive Manufacturing: Discrete Element Simulations of Polyamide 11 and Polyamide 12." *Additive Manufacturing* 36: 101421. doi:10.1016/j.addma.2020.101421.

Steuben, J. C., A. P. Iliopoulos, and J. G. Michopoulos. 2016. "Discrete Element Modeling of Particle-Based Additive Manufacturing Processes." *Computer Methods in Applied Mechanics and Engineering* 305: 537–561. doi:10.1016/j.cma.2016.02.023.

Tan, L. J., W. Zhu, and K. Zhou. 2020. "Recent Progress on Polymer Materials for Additive Manufacturing." *Advanced Functional Materials* 30 (43): 2003062. doi:10.1002/adfm.202003062.

Tan, P., R. Kiran, and K. Zhou. 2021. "Effects of sub-Atmospheric Pressure on Keyhole Dynamics and Porosity in Products Fabricated by Selective Laser Melting." *Journal of Manufacturing Processes* 64: 816–827. doi:10.1016/j.jmapro.2021.01.058.

Tan, P., F. Shen, B. Li, and K. Zhou. 2019. "A Thermo-Metallurgical-Mechanical Model for Selective Laser Melting of Ti6Al4 V." *Materials & Design* 168: 107642. doi:10.1016/j.matdes.2019.107642.

Tangri, H., Y. Guo, and J. S. Curtis. 2017. "Packing of Cylindrical Particles: DEM Simulations and Experimental Measurements." *Powder Technology* 317: 72–82. doi:10.1016/j.powtec.2017.03.058.

Thornton, C., S. J. Cummins, and P. W. Cleary. 2013. "An Investigation of the Comparative Behaviour of Alternative Contact Force Models During Inelastic Collisions." *Powder Technology* 233: 30–46. doi:10.1016/j.powtec.2012.08.012.

Tian, J., E. Liu, and C. He. 2020. "Shear Band Analysis of Granular Materials Considering Effects of Particle Shape." *Acta Mechanica* 231 (11): 4445–4461. doi:10.1007/s00707-020-02771-y.

Tsuji, Y., T. Tanaka, and T. Ishida. 1992. "Lagrangian Numerical Simulation of Plug Flow of Cohesionless Particles in a Horizontal Pipe." *Powder Technology* 71 (3): 239–250. doi:10.1016/0032-5910(92)88030-l.

Türk, D.-A., F. Brenni, M. Zogg, and M. Meboldt. 2017. "Mechanical Characterization of 3D Printed Polymers for Fiber Reinforced Polymers Processing." *Materials & Design* 118: 256–265. doi:10.1016/j.matdes.2017.01.050.

Václav Šmilauer, E. C., and Bruno Chareyre. 2019. "Yade Documentation.".

Wu, H., J. Ren, Q. Huang, X. Zai, L. Liu, C. Chen, S. Liu, X. Yang, and R. Li. 2017. "Effect of Laser Parameters on Microstructure, Metallurgical Defects and Property of AlSi10Mg Printed by Selective Laser Melting." *Journal of Micromechanics and Molecular Physics* 02 (04),.

Xiang, Z., M. Yin, Z. Deng, X. Mei, and G. Yin. 2016. "Simulation of Forming Process of Powder Bed for Additive Manufacturing." *Journal of Manufacturing Science and Engineering* 138 (8), doi:10.1115/1.4032970.

Yu, W., S. L. Sing, C. K. Chua, and X. Tian. 2019. "Influence of re-Melting on Surface Roughness and Porosity of AlSi10Mg Parts Fabricated by Selective Laser Melting." *Journal of Alloys and Compounds* 792: 574–581. doi:10.1016/j.jallcom.2019.04.017.

Yu, W. H., S. L. Sing, C. K. Chua, C. N. Kuo, and X. L. Tian. 2019. "Particle-reinforced Metal Matrix Nanocomposites Fabricated by Selective Laser Melting: A State of the art Review." *Progress in Materials Science* 104: 330–379. doi:10.1016/j.pmatsci.2019.04.006.

Yuan, S., C. K. Chua, and K. Zhou. 2019. "3D-Printed Mechanical Metamaterials with High Energy Absorption." *Advanced Materials Technologies* 4 (3), doi:10.1002/admt.201800419.

Yuan, S., F. Shen, C. K. Chua, and K. Zhou. 2019. "Polymeric Composites for Powder-Based Additive Manufacturing: Materials and Applications." *Progress in Polymer Science* 91: 141–168. doi:10.1016/j.progpolymsci.2018.11.001.

Ziegelmeier, S., P. Christou, F. Wöllecke, C. Tuck, R. Goodridge, R. Hague, E. Krampe, and E. Wintermantel. 2015. "An Experimental Study Into the Effects of Bulk and Flow Behaviour of Laser Sintering Polymer Powders on Resulting Part Properties." *Journal of Materials Processing Technology* 215: 239–250. doi:10.1016/j.jmatprotec.2014.07.029.

Zohdi, T. I. 2013. "Rapid Simulation of Laser Processing of Discrete Particulate Materials." *Archives of Computational Methods in Engineering* 20 (4): 309–325. doi:10.1007/s11831-013-9092-6.